Supporting Information

Gupta et al. 10.1073/pnas.1422800112

SI Text

Preparative Methods

All reagents were purchased from commercial sources and used as received, unless otherwise noted. Solvents were sparged with argon and dried over columns containing Q-5 and molecular sieves. DMF was stored over activated 4-Å molecular sieves for 2 d in a Vacuum Atmospheres drybox under an Ar atmosphere and then decanted onto a second portion of 4-Å molecular sieves for 2 d before use. The syntheses of metal complexes were conducted in an Ar atmosphere. The preparation of $K_2[Mn^{II}H_3buea(OH)]$, $K_2[Mn^{III}H_3buea(O)]$, $K[Mn^{III}H_3buea(OH)]$, $[Mn^{V}H_3buea(O)]$, and ferrocenium tetrafluoroborate ($[FeCp_2]BF_4$) followed the literature procedure (1–4). The $[Mn^{V}H_3buea(^{17}O)]$ samples were prepared from $[Mn^{III}H_3buea(^{17}O)]$ that are synthesized using $H_2{}^{17}O$ (60% enriched). The preparation of EPR samples followed the literature procedure (3).

Preparation of XAS samples.

$[Mn^{III}H_3buea(O)]^{2-}$. A solution of $K_2[Mn^{III}H_3buea(O)]$ (25 μmol, 500 μL of a 50-mM solution in DMF) containing 2 eq of 18-Crown-6 (50 μmol, 13.2 mg) was combined with THF (500 μL) and cooled at −80 °C under argon in a drybox cold well. A portion of the solution was then transferred anaerobically to a precooled XAS sample holder and frozen in liquid N_2.

$[Mn^{IV}H_3buea(O)]^{-}$. A solution of $K_2[Mn^{III}H_3buea(O)]$ (25 μmol, 250 μL of a 100-mM solution in DMF) containing 2 eq of 18-Crown-6 (50 μmol, 13.2 mg) was combined with THF (500 μL) and cooled at −80 °C under argon in a drybox cold well. The solution was then treated with 1 eq of $[Cp_2Fe]BF_4$ solution (25 μmol, 250 μL of a 100-mM solution in DMF), resulting in a color change from red-purple to dark green. After mixing for 2 min, a portion of the solution was transferred anaerobically to a precooled XAS sample holder and frozen in liquid N_2.

$[Mn^{V}H_3buea(O)]$. A solution of $K_2[Mn^{III}H_3buea(O)]$ (25 μmol, 250 μL of a 100-mM solution in DMF) containing 2 eq of 18-Crown-6 (50 μmol, 13.2 mg) was combined with THF (500 μL) and cooled at −80 °C under argon in a drybox cold well. The solution was then treated with 2 eq of $[Cp_2Fe]BF_4$ solution (50 μmol, 250 μL of a 200-mM solution in DMF), resulting in a color change from red-purple to dark brown. After mixing for 2 min, a portion of the solution was transferred anaerobically to a precooled XAS sample holder and frozen in liquid N_2.

Physical Methods

EPR Spectroscopy. X-band (9.6 GHz) and S-band (3.5 GHz) EPR spectra were recorded on a Bruker spectrometer equipped with Oxford liquid helium cryostats. Q-band (34.0 GHz) EPR spectra were recorded on a Bruker spectrometer with a home-built microwave probe and cryostat (5). The quantification of all signals is relative to a CuEDTA spin standard. The concentration of the standard was derived from an atomic absorption standard (Aldrich). For all instruments, the microwave frequency was calibrated with a frequency counter and the magnetic field with a NMR gaussmeter. A modulation frequency of 100 kHz was used for all EPR spectra. The EPR simulation software (*SpinCount*) was written by one of the authors (6). The software diagonalizes the electronic spin Hamiltonian $H = \beta_e \mathbf{B}\cdot\mathbf{g}\cdot\mathbf{S} + \mathbf{S}\cdot\mathbf{D}\cdot\mathbf{S}$, where S is the total spin of the complex unless explicitly stated and the parameters have the usual definitions. The hyperfine term ($\mathbf{S}\cdot\mathbf{A}\cdot\mathbf{I}$) is treated as a perturbation in second order for the energies of the spin states. The linewidth of the spectra is dominated by a distribution in the rhombicity E/D, where 1 SD in the distribution is $\sigma_{E/D}$. The quantitative simulations are least-squares fits of the experimental spectra generated with consideration of all intensity factors, which allows computation of simulated spectra for a specified sample concentration.

X-Ray Absorption Spectroscopy. X-ray absorption spectra were collected at the Stanford Synchrotron Radiation Lightsource (SSRL) on beamline 7–3 at an electron energy of 3.0 GeV with an average current of 300 mA. The incoming X-ray was monochromatized by a Si(220) double-crystal monochromator. The intensity of the incident X-ray was monitored by an N_2-filled ion chamber (I_0) in front of the sample. Solution samples were filled in 40-μL plexiglass holders and kept under liquid N_2 until data collection. Data were collected as fluorescence excitation spectra with a Ge 30 element detector (Canberra). The monochromator energy was calibrated by the preedge peak top of $KMnO_4$ standard at 6543.30 eV. The standard was placed between two N_2-filled ionization chambers (I_1 and I_2) after the sample. All data were collected at 8 K, using a liquid He flow cryostat (Oxford). The X-ray flux of 1×10^7 photons per square micrometer on the sample was used for the data collection, which is similar to the number used for collecting the data of biological samples (Photosystem II). This number was determined to be nondamaging on the basis of detailed radiation-damage studies of PSII solution samples (7, 8). In addition, we have done several scans at the same sample spot and did not observe a noticeable Mn XANES edge shift.

Data reduction of the extended X-ray absorption fine structure (EXAFS) spectra was performed using SixPack (Samuel Webb, SSRL). Preedge and postedge backgrounds were subtracted from the XAS spectra, and the results were normalized with respect to edge height. Background removal in k space was achieved through a five-domain cubic spline. Curve fitting was performed with Artemis and IFEFFIT software, using ab initio-calculated phases and amplitudes from the program FEFF 8.2 (9, 10). These ab initio phases and amplitudes were used in the EXAFS equation:

$$\chi(k) = S_0^2 \sum_j \frac{N_j}{k R_j^2} f_{\mathrm{eff}_j}(\pi, k, R_j) e^{-2\sigma_j^2 k^2} e^{-2R_j/\lambda_j(k)} \sin\left(2kR_j + \phi_{ij}(k)\right). \quad [S1]$$

The neighboring atoms to the central atom(s) are divided into j shells, with all atoms with the same atomic number and distance from the central atom grouped into a single shell. Within each shell, the coordination number N_j denotes the number of neighboring atoms in shell j at a distance of R_j from the central atom. The $f_{\mathrm{eff}_j}(\pi, k, R_j)$ term is the ab initio amplitude function for shell j, and the Debye–Waller term $e^{-2\sigma j 2k2}$ accounts for damping due to static and thermal disorder in absorber-backscatterer distances. The mean free path term $e^{-2Rj/\lambda j(k)}$ reflects losses due to inelastic scattering, where $\lambda_j(k)$ is the electron mean free path. The oscillations in the EXAFS spectrum are reflected in the sinusoidal term, $\sin(2kR_j + \varphi_{ij}(k))$, where $\varphi_{ij}(k)$ is the ab initio phase function for shell j. $S_0{}^2$ is an amplitude reduction factor due to shake-up/shake-off processes at the central atom (s). The EXAFS equation was used to fit the experimental data using N, R, and the EXAFS Debye–Waller factor (σ^2) as variable parameters. E_0 was defined as 6545.0 eV and the $S_0{}^2$ value was fixed to 0.85 for the energy (eV) to wave vector (k, Å^{-1}) axis conversion.

Mn XANES preedge spectra were fitted using EDG_FIT in EXAFSPAK (11). Preedge spectra were fitted with a pseudo-Voigt line with a 1:1 ratio of Lorentzian and Gaussian functions. The number of the preedge components and their positions were estimated by the second derivative spectra. Some data for Table S1 are taken from previous reports (12, 13).

Computational Methods. The DFT calculations were performed with the program suit Gaussian 09 (14), using the functional B3LYP and the basis set 6-311G. The self-consistent field (SCF) procedure and geometry optimizations used default settings for the convergence criteria. The magnetic hyperfine parameters A^{SD} and A^{FC} were evaluated with the properties package of G09 and discussed using Mulliken population analysis. The spin density contour plots in Fig. 5 were obtained using the graphics program GaussView (15).

The Mn–oxo bonds in the series of $[Mn^{n}H_3buea(O)]^{m}$ complexes are best described as having a bond order of 2, in which an empty z^2 orbital and two half-filled xz and yz orbitals are involved in the bonding. However, this description is an idealization, and closer inspection of the calculations showed that the {xz, yz} orbitals are slightly admixed with those of the $\{x^2\text{-}y^2, xy\}$ set due to the displacement of the Mn centers from the trigonal plane toward the oxido ligand. Consequently, this admixture is allowed in $[Mn^{III}H_3buea(O)]^{2-}$ and $[Mn^{V}H_3buea(O)]$, which have C_3 symmetry, and $[Mn^{IV}H_3buea(O)]^{-}$, which has lower symmetry. The out-of-plane shift of the Mn ion becomes smaller as the oxidation state of the Mn center is increased, resulting in a shortening of the $Mn–N_{urea}$ bonds. For example, the out-of-plane distance shifts from 0.34 Å to 0.28 Å upon oxidation of $[Mn^{III}H_3buea(O)]^{2-}$ to $[Mn^{IV}H_3buea(O)]^{-}$. This trend is similar to the one observed in the related $[Fe^{III}H_3buea(O)]^{2-}$ and $[Fe^{IV}H_3buea(O)]^{-}$, which was confirmed with XRD measurements (16).

1. Gupta R, MacBeth CE, Young VG, Jr, Borovik AS (2002) Isolation of monomeric Mn (III/II)-H and Mn(III)-complexes from water: Evaluation of O-H bond dissociation energies. *J Am Chem Soc* 124(7):1136–1137.
2. MacBeth CE, et al. (2004) Utilization of hydrogen bonds to stabilize M-O(H) units: Synthesis and properties of monomeric iron and manganese complexes with terminal oxo and hydroxo ligands. *J Am Chem Soc* 126(8):2556–2567.
3. Taguchi T, et al. (2012) Preparation and properties of a monomeric high-spin Mn(V)-oxo complex. *J Am Chem Soc* 134(4):1996–1999.
4. Connelly NG, Geiger WE (1996) Chemical redox agents for organometallic chemistry. *Chem Rev* 96(2):877–910.
5. Petasis DT, Hendrich MP (1999) A new Q-band EPR probe for quantitative studies of even electron metalloproteins. *J Magn Reson* 136(2):200–206.
6. Golombek AP, Hendrich MP (2003) Quantitative analysis of dinuclear manganese(II) EPR spectra. *J Magn Reson* 165(1):33–48.
7. Yano J, et al. (2005) X-ray damage to the Mn_4Ca complex in single crystals of photosystem II: A case study for metalloprotein crystallography. *Proc Natl Acad Sci USA* 102(34):12047–12052.
8. Glöckner C, et al. (2013) Structural changes of the oxygen-evolving complex in photosystem II during the catalytic cycle. *J Biol Chem* 288(31):22607–22620.
9. Newville M (2001) IFEFFIT: Interactive XAFS analysis and FEFF fitting. *J Synchrotron Radiat* 8(Pt 2):322–324.
10. Rehr JJ, Albers RC (2000) Theoretical approaches to X-ray absorption fine structure. *Rev Mod Phys* 72(3):621–654.
11. George GN (1990) *EXAFSPAK* (Stanford Synchrotron Radiation Laboratory, Stanford, CA).
12. Taguchi T, et al. (2014) Preparation and properties of an Mn^{IV}-hydroxide complex: Proton and electron transfer at a mononuclear manganese site and its relationship to the oxygen evolving complex within photosystem II. *Chem Sci* 5(8):3064–3071.
13. Yano J, et al. (2007) Polarized X-ray absorption spectroscopy of single-crystal Mn(V) complexes relevant to the oxygen-evolving complex of photosystem II. *J Am Chem Soc* 129(43):12989–13000.
14. Frisch MJ, et al. (2010) *Gaussian 09, Revision B.01* (Gaussian, Wallingford CT).
15. Dennington R, Keith T, Millam J (2009) *GaussView 5.0.8* (Semichem Inc., Shawnee Mission, KS).
16. Lacy DC, et al. (2010) Formation, structure, and EPR detection of a high spin $Fe^{(IV)}$-oxo species derived from either an $Fe^{(III)}$-oxo or $Fe^{(III)}$-OH complex. *J Am Chem Soc* 132(35):12188–12190.

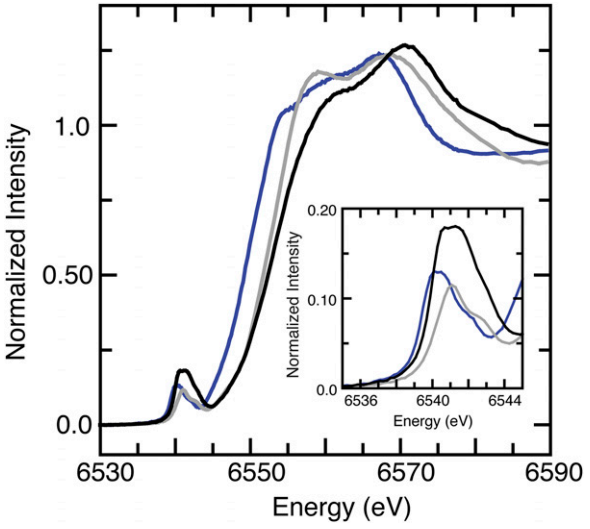

Fig. S1. XANES results for the $[Mn^{n}H_3buea(O)]^{m}$ complexes: $[Mn^{III}H_3buea(O)]^{2-}$ (blue), $[Mn^{IV}H_3buea(O)]^{-}$ (gray), and $[Mn^{V}H_3buea(O)]$ (black). *Inset* shows the zoomed-in view of the XANES preedge region. A small amount of $[Mn^{IV}H_3buea(O)]^{-}$ (~10%) was present in the sample that was determined by EPR spectroscopy—this amount was subtracted from the spectrum before analysis.

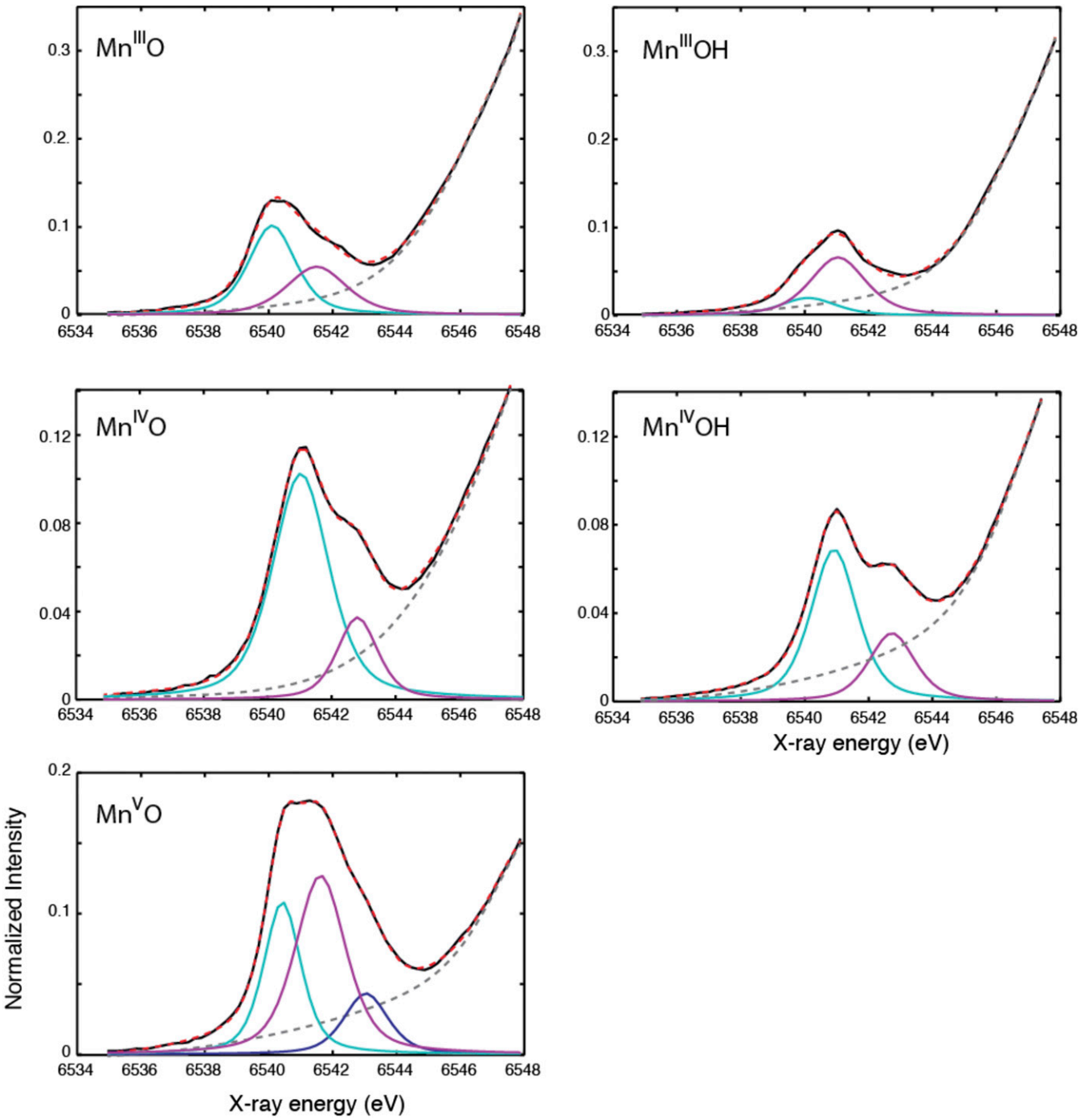

Fig. S2. Preedge curve fits of Mn oxo and hydroxo compounds: black solid line, experimental data; red dotted line, fit; light blue, purple, and dark blue lines, preedge peak components listed in Table S1. Gray dotted lines are the background.

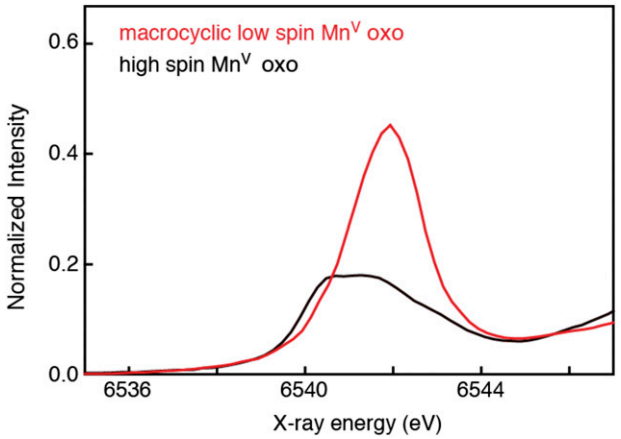

Fig. S3. A comparison of the preedge spectra of [Mn^{V}H$_3$buea(O)] (black) and low-spin [Mn^{V}TAML(O)]$^{-}$ complex (red) (13).

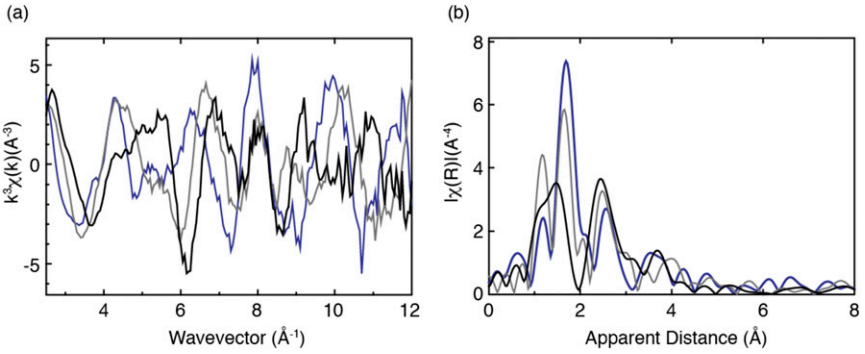

Fig. S4. (*A*) k^3-weighted Mn EXAFS spectra of [Mn^{III}H$_3$buea(O)]$^{2-}$ (blue), [Mn^{IV}H$_3$buea(O)]$^{-}$ (gray), and [Mn^{V}H$_3$buea(O)] (black) and (*B*) their Fourier transformed spectra. For the [Mn^{V}H$_3$buea(O)] spectrum, a contribution of ~10% Mn^{IV}-O was subtracted (determined from EPR measurements). For *B*, the *k* space of 2.7–11.9 Å^{-1} was used for [Mn^{III}H$_3$buea(O)]$^{2-}$ and [Mn^{IV}H$_3$buea(O)]$^{-}$ and 3.0–11.2 Å^{-1} for [Mn^{V}H$_3$buea(O)].

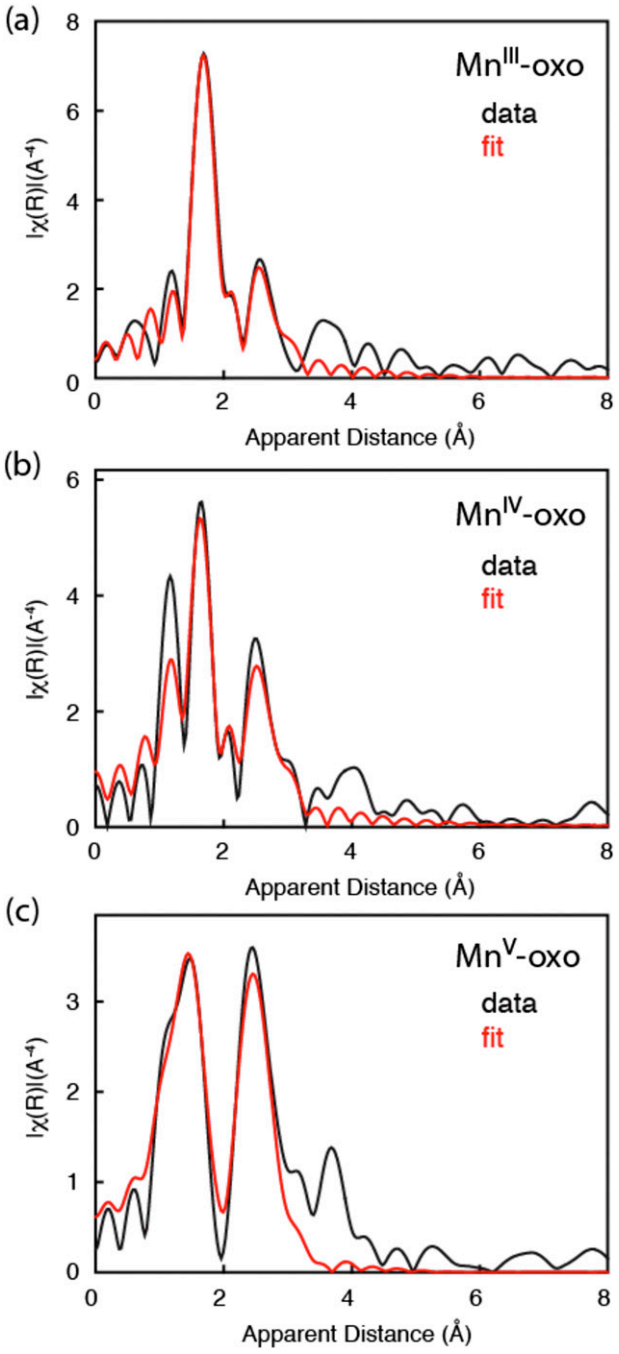

Fig. S5. Mn EXAFS curve-fitting results for (*A*) $[Mn^{III}H_3buea(O)]^{2-}$, (*B*) $[Mn^{IV}H_3buea(O)]^{-}$, and (*C*) $[Mn^{V}H_3buea(O)]$. The fit range was 2.7–11.9 $Å^{-1}$ for $[Mn^{III}H_3buea(O)]^{2-}$, 2.7–11.9 $Å^{-1}$ for $[Mn^{IV}H_3buea(O)]$–, and 3.0–11.2 $Å^{-1}$ for $[Mn^{V}H_3buea(O)$. The detailed fitting parameters are shown in Table S2.

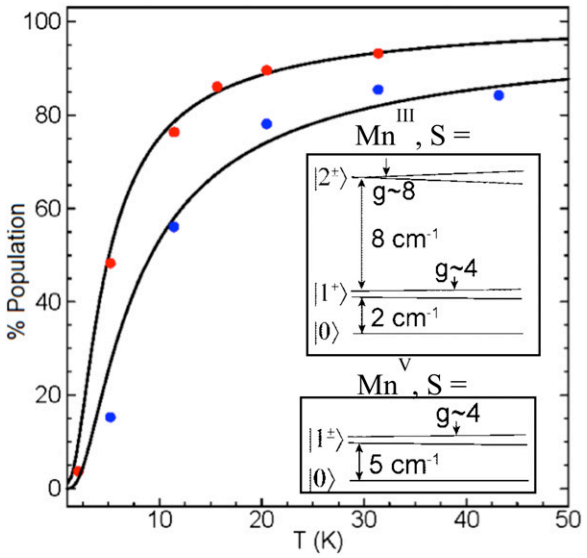

Fig. S6. Signal intensity times temperature vs. temperature of the g = 8.08 (blue) and g = 4.01 (red) EPR signals of $[Mn^{III}H_3buea(O)]^{2-}$ and $[Mn^{V}H_3buea(O)]$, respectively. The black lines are the theoretical percentage of population of the $|2\pm\rangle$ (S = 2) and $|1\pm\rangle$ (S = 1) doublets for the D values given in Table 2. *Inset* shows schematic energy levels of the S = 2 and 1 spin states.

Table S1. Preedge energy and area of Mn–oxo and hydroxo compounds

Compound	Preedge energy, eV	Peak height	Total peak area
Mn–oxo			
$Mn^{III}O$	6,540.1	0.10	0.37
	6,541.5	0.05	
$Mn^{IV}O$	6,541.0	0.10	0.33
	6,542.8	0.04	
$Mn^{V}O$	6,540.4	0.11	0.57
	6,541.6	0.13	
	6,543.0	0.04	
Low-spin $Mn^{V}O^{\dagger}$	6,540.8	0.14	1.10
	6,541.6	0.35	
Mn–OH*			
$Mn^{III}OH$	6,540.1	0.02	0.22
	6,541.0	0.07	
$Mn^{IV}OH$	6,540.9	0.07	0.21
	6,542.7	0.03	

*Data are from ref. 12.
†A low-spin Mn^{V}–oxo compound taken from ref. 13.

Table S2. Listing of EXAFS curve-fitting parameters obtained for the $[Mn^nH_3buea(O)]^m$ complexes, together with the distances obtained from DFT and XRD

			Distances, Å				
n	Shell	N	DFT	XRD	EXAFS	σ^2, Å*	R, %†
III	Mn–O	1	1.77	1.77	1.78 (0.02)	0.002 (0.001)	1.2
	Mn–N	4	2.12	2.05–2.14	2.07 (0.02)	0.003 (0.001)	E_0 (eV) = 7.3
	Mn–C	9		2.92–3.15	2.99 (0.04)	0.017 (0.004)	
	Mn–N	3		3.27–3.34	3.30 (0.05)	0.004 (0.001)	
	Mn–CN	18		3.25–3.31	3.22 (0.06)	0.005 (0.001)	
IV	Mn–O	1	1.71		1.76 (0.03)	0.002 (0.001)	4.9
	Mn–N	4	2.02		2.00 (0.02)	0.004 (0.002)	E_0 (eV) = 4.9
	Mn–C	9			2.92 (0.05)	0.015 (0.005)	
	Mn–N	3			3.27 (0.06)	0.004 (0.001)	
	Mn–CN	18			3.16 (0.09)	0.005 (0.003)	
V	Mn–O	1	1.68		1.68 (0.04)	0.005 (0.011)	11.0
	Mn–N	4	1.95		1.86 (0.05)	0.005 (0.005)	E_0 (eV) = 0.7
	Mn–C	9			2.86 (0.12)	0.011 (0.010)	
	Mn–N	3			3.24 (0.14)	0.004 (0.001)	
	Mn–CN	18			3.28 (0.18)	0.005 (0.001)	

Values in parentheses are the errors associated with the measurement.
*σ^2 is the Debye–Waller factor.
†R, % shows the goodness of fit.

Table S3. Listing of angular data obtained from DFT for the $[Mn^nH_3buea(O)]^m$ complexes

n	III	IV*	V
N–Mn–N′, °	117	108, 111, 134	118
$\Delta_{out\text{-}of\text{-}plane}$, Å†	0.34	0.28	0.24

*Jahn–Teller distorted structure due to partial occupation of E{x (2)-y (2), xy} that results in considerable dπ–dδ orbital mixing.
†Distance between Mn and trigonal plane formed by the three urea N atoms.